J. Plasma Physics (2015), *vol.* 81, 365810201 © Cambridge University Press 2014
doi:10.1017/S0022377814001093

Magnetic-field generation by the ablative nonlinear Rayleigh–Taylor instability

Philip M. Nilson[1,2]†, L. Gao[1,3]‡, I. V. Igumenshchev[1], G. Fiksel[1], R. Yan[1,2,3], J. R. Davies[1,2,3], D. Martinez[4], V. A. Smalyuk[4], M. G. Haines[5]¶, E. G. Blackman[1,6], D. H. Froula[1], R. Betti[1,2,3,6] and D. D. Meyerhofer[1,2,3,6]

[1]Laboratory for Laser Energetics, University of Rochester, Rochester, NY 14623, USA
[2]Fusion Science Center, University of Rochester, Rochester, NY 14623, USA
[3]Department of Mechanical Engineering, University of Rochester, Rochester, NY 14623, USA
[4]Lawrence Livermore National Laboratory, Livermore, California 94550, USA
[5]Department of Physics, Imperial College, London SW7 2AZ, United Kingdom
[6]Department of Physics, University of Rochester, Rochester, NY 14623, USA

(Received 28 May 2014; revised 9 September 2014; accepted 24 October 2014; first published online 3 December 2014)

Experiments reporting magnetic-field generation by the ablative nonlinear Rayleigh–Taylor (RT) instability are reviewed. The experiments show how large-scale magnetic fields can, under certain circumstances, emerge and persist in strongly driven laboratory and astrophysical flows at drive pressures exceeding one million times atmospheric pressure.

1. Introduction

From inertial confinement fusion (ICF) (Lindl 1995; Atzeni 2004) to supernova hydrodynamics (Remington et al. 1997) and galactic dynamos (Kulsrud and Zweibel 2008), understanding the effects of hydrodynamic instability growth on strongly driven flows is a major open problem (Orszag and Patterson 1972; Schneider et al. 1998; Dimotakis 2000; Drake 2006). Unlike neutral fluids, hydrodynamic instability growth in conducting plasmas can produce seed vorticity that generates magnetic fields (Mima et al. 1978; Evans 1986). The challenge, in a large number of cases, is to understand how the magnetic seed field grows when the thermal and flow pressures dominate the magnetic pressure. In high-energy-density conditions, little magnetic-field data exist and techniques are widely sought for testing magnetohydrodynamic (MHD) model predictions (Srinivasan et al. 2012). Such experimental tests are important for developing an understanding of the flow-driven processes that can generate large-scale magnetic-field structures in a wide variety of laboratory and astrophysical systems (Remington et al. 1997; Drake 2006).

This review describes some of the first laboratory experiments to investigate magnetic-field generation during hydrodynamic instability growth inside a strongly driven plasma (Gao et al. 2012, 2013). The work presented here used the RT instability (Rayleigh 1883; Taylor 1950) and the large thrust (ablation pressure) that can be generated when a high-energy laser ablates a solid target. In these systems, where the thermal and flow pressures dominate the magnetic pressure, it is shown that

† Email address for correspondence: pnil@lle.rochester.edu
‡ Present address: Department of Astrophysical Sciences, Princeton University, USA
¶ Deceased

https://doi.org/10.1017/S0022377814001093 Published online by Cambridge University Press

large-scale magnetic fields can grow. The measured spatial and temporal evolutions of these magnetic fields are in good agreement with two-dimensional (2D) MHD simulations and bubble competition and merger model predictions (Alon et al. 1994; Oron et al. 1998, 2001), linking the generated magnetic fields with the RT bubble and spike growth.

This manuscript is organized as follows: Sec. 2 briefly reviews laser-driven ablation and RT instability growth at laser-driven ablation fronts; Sec. 3 describes magnetic-field generation during RT instability growth; Sec. 4 describes the experimental setup and the proton radiography diagnostic that was used in this work; Sec. 5 presents results from side-on proton radiography experiments, showing the target dynamics during RT instability growth; Sec. 6 describes results from face-on proton radiography experiments, showing the spatial and temporal evolutions of the RT-generated magnetic fields; Sec. 7 compares the experimental data with bubble competition and merger model predictions; and Sec. 8 provides a summary and conclusions.

2. Laser-driven ablation and RT instability growth

When a high-energy laser irradiates a solid target, the surface is rapidly heated and the low-density ablated plasma pushes on the higher-density material, driving the target forward by rocket reaction. At the target surface, optical laser light propagates inside the ablated plasma up to the critical-density surface where laser-energy deposition occurs. Laser energy is absorbed by collisional and resonance absorption processes, as well as by density perturbations that lead to parametric instabilities (energy can be redistributed in the plasma by coupling scattered-light waves, electron-plasma waves, and ion-acoustic waves). The high-temperature coronal plasma expands under its own pressure and presents an increasing density gradient to the incident laser radiation. Energy absorption at the critical surface generates a stationary ablation front in the deflagration limit, with electron thermal conduction transporting energy from the critical surface to the ablation surface. The target responds to the ablation pressure in a rocket-like fashion and the heated material exerts a pressure on the cooler, higher-density material, launching a shock wave ahead of the electron-driven heat front (Atzeni 2004).

Ablation pressures up to 100 Mbar (100 million times atmospheric pressure) are generated with modern high-energy UV laser systems focused to 10^{15} W cm^{-2}. These ablation pressures accelerate thin solid targets to velocities exceeding 100 km s^{-1} and have been studied intensively because of their relevance to ignition target designs for ICF (Lindl 1995). Under these conditions, accelerated foils are susceptible to RT instability growth, breaking the targets apart into a mass modulated structure that grows in time (Knauer et al. 2000).

The RT instability is buoyancy driven, occurring whenever a fluid supports or accelerates a fluid of higher density in the presence of interfacial perturbations. In the work reviewed here, the target modulations were seeded by laser non-uniformities and amplified during the target's acceleration phase. In the linear regime, each perturbation mode develops independently and grows exponentially. For ablatively driven fronts, the growth rate is reduced or even stabilized (Betti and Sanz 2006). When the mode amplitude becomes comparable to its wavelength, the modulations develop into bubbles and spikes, where less-dense material rises through heavier material and heavier material falls through less-dense material (Smalyuk et al. 2005). In the nonlinear regime, bubbles merge and evolve self-similarly prior to more complex behavior at later times (Alon et al. 1994; Sadot et al. 2005).

https://doi.org/10.1017/S0022377814001093 Published online by Cambridge University Press

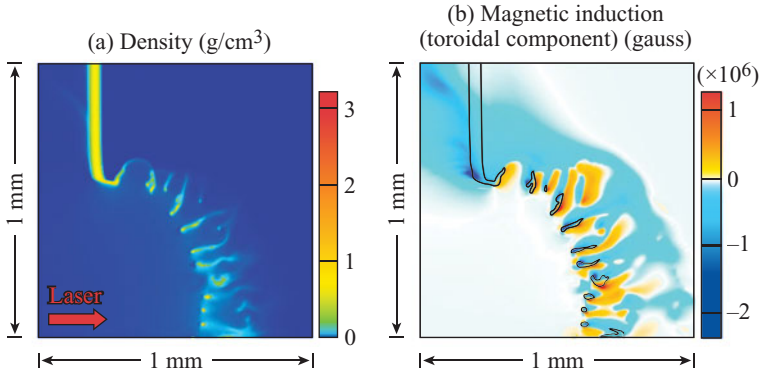


FIGURE 1. Magnetic-field generation during RT instability growth inside a laser-driven plastic target. The calculations were carried out using the 2D resistive MHD code *DRACO* (Keller et al. 1999; Igumenshchev et al. 2009). The laser propagation direction is shown. (a) Density profile at $t = t_0 + 2.1$ ns. The target is axisymmetric about the horizontal axis. (b) Magnetic-field distribution at $t = t_0 + 2.1$ ns. The density contour for $\rho = 0.05$ g cm^{-3} is shown. (Reprinted from Gao et al. (2012) with permission from the American Physical Society. Copyright 2012, APS Publishing LLC.)

3. Magnetic-field generation during RT instability growth

Previous theoretical work showed that a plasma subjected to the RT instability can generate magnetic fields (Mima et al. 1978; Evans 1986). Recently, the first measurements of RT-induced magnetic fields were reported in the linear (Manuel et al. 2012) and nonlinear stages (Gao et al. 2012, 2013). These magnetic fields are generated by the steep, non-collinear density and temperature gradients that form inside the RT-unstable plasma. This process is illustrated for a laser-driven foil by numerical modeling with the 2D resistive MHD code *DRACO* (Keller et al. 1999; Igumenshchev et al. 2009).

In these calculations, the magnetic-field equation is

$$\frac{\partial \mathbf{B}}{\partial t} = \nabla \times (\mathbf{V} \times \mathbf{B}) + \frac{c}{e}\left[\nabla \times \left(\frac{\nabla p_e}{n_e}\right) - \nabla \times \frac{(\nabla \times \mathbf{B}) \times \mathbf{B}}{4\pi n_e} - \nabla \times \frac{\mathbf{R_T} + \mathbf{R_u}}{n_e}\right], \quad (3.1)$$

where $\mathbf{B}$ is the magnetic induction, p_e is the electron pressure, n_e is the electron number density, e is the fundamental unit of charge, $\mathbf{V}$ is the flow velocity, and $\mathbf{R_T}$ and $\mathbf{R_u}$ are the thermal and frictional forces (Braginskii 1965), respectively. $\mathbf{R_T}$ and $\mathbf{R_u}$ were calculated using the full Braginskii transport coefficients (Braginskii 1965), including the Nernst term (Nishiguchi et al. 1985) and cross-gradient thermal fluxes. The non-uniform electron pressure gradient term drives the thermoelectric (Biermann) source of magnetic-field growth (Haines 1986). The RT instability growth was seeded in these calculations by an imposed 50 μm-wavelength target perturbation with 1 μm peak-to-valley amplitude. This mode grew the fastest when the simulation was initialized without any preimposed modulations and the final perturbations grew from numerical noise.

Figure 1 shows *DRACO* calculations for a 15 μm-wavelength CH (plastic) foil irradiated with a 2.5 ns laser pulse focused to 4×10^{14} W cm^{-2}. These calculations were carried out in 2D cylindrical geometry. Figure 1(a) shows the calculated target-density profile at $t = t_0 + 2.1$ ns, where t_0 is the arrival time of the long-pulse beams at the target surface. The calculations show density modulations that have grown due

https://doi.org/10.1017/S0022377814001093 Published online by Cambridge University Press

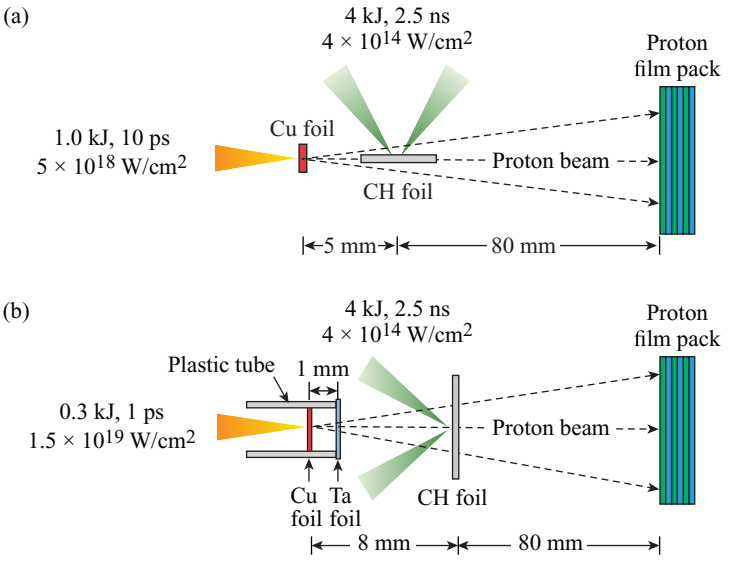


FIGURE 2. Experimental setup. Side-on (a) and face-on (b) proton radiography geometries.

to the RT instability, breaking the target apart during the acceleration phase. The target is accelerated from left to right.

Figure 1(b) shows the calculated magnetic-field distribution. The position of the target is indicated by the overlaid density contour for 0.05 g cm^{-3}. At this time, megagauss-level magnetic fields are predicted. The data show magnetic fields generated at the ablation surface that are convected toward the corona by the ablated-plasma flow and to higher-density regions by hot electrons that carry the heat flux (the Nernst effect) (Nishiguchi et al. 1985). The magnitude of the calculated magnetic fields is not dynamically significant and has little or no effect on the RT instability growth in the linear and moderately nonlinear stages.

In practice, the magnetic-field lines wrap around the RT bubbles and spikes. Bubbles and spikes form where light material rises into dense material and dense material falls through light material. The non-uniform electron pressure gradient term induces poloidal current loops that wrap around the magnetic-field toroids. Even though the full three-dimensional (3D) nature of the problem is not captured by the *DRACO* calculations, the magnitude and predominant wavelength of the predicted magnetic fields are expected to be accurate.

4. Experimental setup

The experiments were carried out on the OMEGA EP Laser Facility (Waxer et al. 2005) at the University of Rochester's Laboratory for Laser Energetics (LLE). Planar target foils were irradiated with two high-energy laser pulses focused to more than 10^{14} W cm^{-2}. Figure 2 shows the experimental setup. The main target foils were 15 or 25 μm thick CH foils, 5 × 5 mm^2 in area. Each laser pulse delivered 2 kJ of laser energy at a wavelength of 351 nm and had a 2.5 ns square temporal profile, co-timed to arrive at the target at t_0. The laser pulses irradiated the main target at a 23° angle of incidence to the target normal. The laser beams used distributed phase plates (LLE 1987) and were focused to 850 μm-diam focal spots, providing an overlapped laser intensity of 4 × 10^{14} W cm^{-2}.

https://doi.org/10.1017/S0022377814001093 Published online by Cambridge University Press

The MHD response of the plasma to the RT instability growth was measured using ultrafast laser-driven proton radiography (Borghesi et al. 2004; Cowan et al. 2004). Figures 2(a) and (b) show the side-on and face-on proton radiography geometries, respectively, that were used in this study. The proton source was generated by irradiating a 20 μm-thick Cu foil with a 1 kJ, 10 ps pulse focused to 5×10^{18} W cm^{-2} or a 300 J, 1 ps pulse focused to 1.5×10^{19} W cm^{-2}. The high-intensity laser pulse had a wavelength of 1.053 μm. The protons were derived from hydrocarbon contaminants on the rear surface of the foil and accelerated by target-normal sheath fields (Wilks et al. 2001). The proton-source foil was located in a plastic tube with a 5 μm-thick Ta foil mounted on the side facing the main target interaction. This assembly protected the Cu foil from the radiation and the ablated-plasma flow that was generated by the main target. Protecting the proton-source foil was important because radiation preheat and plasma flow reaching the Cu target could disrupt the target-normal sheath acceleration mechanism and prevent proton acceleration (Zylstra et al. 2012).

The time-of-flight effects of the broadband, subrelativistic-proton source made it possible to obtain a series of time-resolved proton radiographs on each shot. This measurement was achieved by employing a stack of filtered radiochromic film (RCF) as a dosimetric detector. Protons with different energies deposited energy in different RCF layers, providing radiographs of the main target interaction at different times. Electromagnetic field deflections at the main target gave rise to variations in the spatial distribution of proton energy deposition on each film layer. In these experiments, collisional scattering and stopping in the main target were negligible. The image magnification was $M = (L + l)/l$, where l was the distance between the proton-source foil and the main target and L was the distance from the main target to the RCF detector. The image magnification M was 17–20 for the side-on radiography measurements and 11–13 for the face-on radiography measurements. For each configuration, the range of magnifications depends on the depth of the RCF layer inside the filtered stack detector. The spatial and temporal resolutions obtained in these experiments were between 5 and 10 μm and a few picoseconds, respectively.

Figure 3 shows typical examples of proton-energy spectra from Cu targets driven with 40, 680, and 982 J, 10 ps pulses. The energy spectra of the forward-accelerated proton beams were measured using the nuclear activation of copper stacks (Clark 2001; Willingale et al. 2009). Proton-beam spatial profiles are shown for 8, 15, and 24 MeV protons from the highest-energy interaction. RT-unstable targets were not used in any of these measurements.

5. Target dynamics during RT instability growth

Figure 4 shows a side-on proton radiograph of a 25 μm-thick CH foil at $t = t_0 + 2.56$ ns taken with 13 MeV protons. The central part of the foil traveled from left to right. The horizon created by the foil outside of the laser focal region is shown. The driven foil is clearly observed in the radiographic image and is unbroken by RT instability growth. Based on the trajectory history, the velocity of the driven foil is $(3 \pm 1) \times 10^7$ cm s^{-1}.

Figures 5(a) and (b) show side-on proton radiographs of a 15 μm-thick CH foil at times $t = t_0 + 2.11$ ns and $t = t_0 + 2.56$ ns, respectively. The data were measured using two different shots with the same laser-drive conditions as used in the thicker-target case. The radiographs were obtained with 13 MeV proton energies. Because collisional scattering and stopping of the proton probe beam are insignificant inside the main target, the broken-target dynamics are revealed in the proton radiography data by

https://doi.org/10.1017/S0022377814001093 Published online by Cambridge University Press

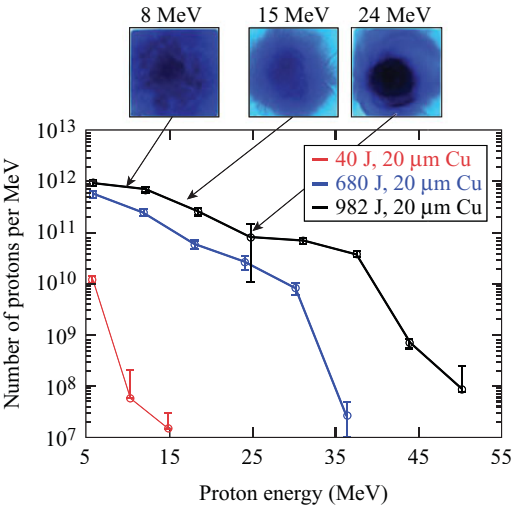


FIGURE 3. Example proton-energy spectra and proton-beam profiles generated from Cu-foil target interactions driven by 10 ps pulses.

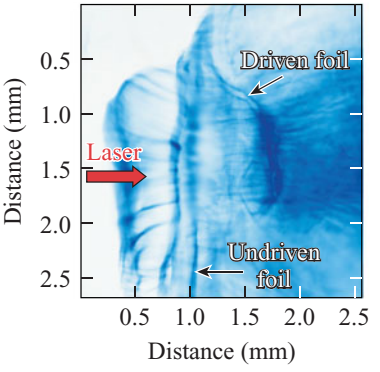


FIGURE 4. Stable target. Side-on proton radiograph of a 25 μm-thick CH foil taken with 13 MeV protons at time $t = t_0 + 2.56$ ns. The laser drive, the undriven foil horizon, and the driven foil are shown. (Reprinted from Gao et al. (2012) with permission from the American Physical Society. Copyright 2012, APS Publishing LLC.)

the electromagnetic fields that were generated at the RT-unstable interface. The data show the appearance of bubble-like cellular structures. At later times, larger-scale structures reveal the growth of these features, consistent with the target breaking apart during the acceleration phase. Figure 5(b) shows a plasma sheath ahead of the RT-unstable plasma. This sheath field was likely caused by plasma feeding through the RT-unstable interface, providing further evidence for the compromised foil. This effect is not observed in the case of the 25 μm-thick CH foil in Fig. 4.

6. Spatial and temporal evolution of the RT-generated magnetic fields

Detailed maps of the RT-generated magnetic fields were measured using the face-on proton radiography geometry shown in Fig. 2(b). Figure 6 shows face-on proton radiographs of the magnetic-field structures that grew as the target was accelerated. Figures 6(a) and (c) show data for 15 μm-thick CH targets at $t = t_0 + 2.12$ ns

https://doi.org/10.1017/S0022377814001093 Published online by Cambridge University Press

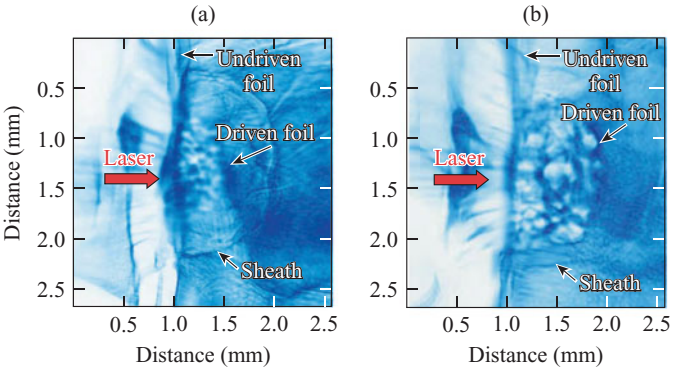


FIGURE 5. RT-unstable targets. Side-on proton radiographs of 15 μm-thick CH foils taken with 13 MeV protons at (a) $t = t_0 + 2.11$ ns and (b) $t = t_0 + 2.56$ ns. The laser drive, the undriven foil horizon, the RT-unstable plasma, and the plasma sheath are shown. (Reprinted from Gao et al. (2012) with permission from the American Physical Society. Copyright 2012, APS Publishing LLC.)

and $t = t_0 + 2.62$ ns. The data show magnetic fields in the RT-unstable plasma deflecting protons and forming cellular structures in the radiography images. These measurements were carried out with 25 MeV protons. The darker regions in the images were created by a higher proton flux, revealing proton-beam deflections at the main target. In the absence of the main-target interaction, a smooth proton-beam profile was measured and no cellular structures were observed.

The formation of sharp cellular structures in proton radiography experiments was previously interpreted as caustics (Kugland et al. 2012). Based on caustic formation in the present experiments, the measured size of the cellular structures at a given time is insensitive to the magnitude of the magnetic field for proton energies above 9 MeV and magnetic fields above 0.5 MG. A detailed description of this process will be given in a future publication (Gao 2014).

The total number of magnetic-field cells and the cell-size distribution was determined as a function of time using the watershed algorithm (Vincent and Soille 1991). Figures 6(b) and (d) show the cells that were identified by this algorithm, overlaid on the original proton radiography data. Based on this analysis, the total number of cells and the cell-size distribution was reconstructed. The cell sizes were calculated from $D = (4S/\pi)^{1/2}$, where S is the cell area.

Figure 7(a) shows the magnetic-field cell-size distributions for four different times taken on different shots. In time, the average magnetic-field cell sizes shifted to longer wavelengths and the total number of magnetic field cells decreased. The average cell sizes $\langle D \rangle$ at different times were determined by fitting the cell-size data with normal distribution functions. For the time intervals shown in Fig. 7(a), the average cell size increased in time from 83 μm to 99 μm, 121 μm, and 143 μm. These values agree with the direct calculations of $\langle D \rangle$ using the cell sizes from the watershed algorithm analysis. Figure 7(b) shows the normalized cell-size distributions as a function of the normalized cell size $D/\langle D \rangle$. The dashed curve is a fit to the experimental data using the Gaussian distribution function

$$f(D/\langle D \rangle) = \frac{1}{\sqrt{2\pi}\,\psi} \exp\left[-\frac{(D/\langle D \rangle - 1)^2}{2\psi^2}\right], \tag{6.1}$$

https://doi.org/10.1017/S0022377814001093 Published online by Cambridge University Press

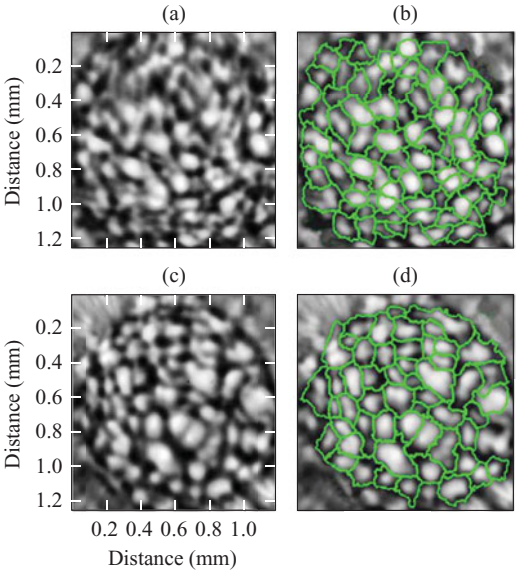


FIGURE 6. Face-on proton radiographs of 15 μm-thick CH foils taken with 13 MeV protons at (a) $t = t_0 + 2.12$ ns and (c) $t = t_0 + 2.62$ ns. (b), (d) Magnetic field cells identified with the watershed algorithm. (Reprinted from Gao et al. (2013) with permission from the American Physical Society. Copyright 2013, APS Publishing LLC.)

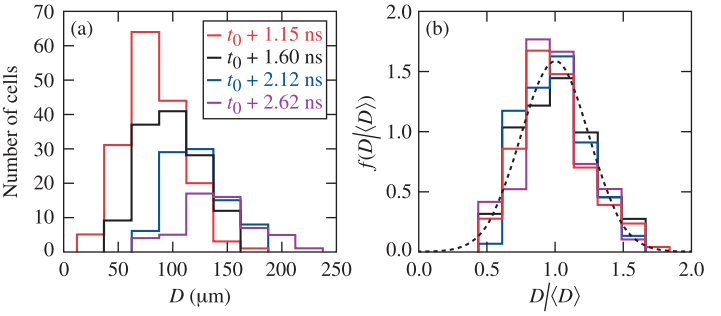


FIGURE 7. (a) Magnetic-field cell-size distributions at four different times (see text for details). (b) Normalized magnetic-field cell-size distributions as a function of the normalized cell size for each of the times shown in (a). (Reprinted from Gao et al. (2013) with permission from the American Physical Society. Copyright 2013, APS Publishing LLC.)

where $\psi = 0.25 \pm 0.10$. This analysis shows that the normalized magnetic-field distributions are time invariant and evolve self-similarly (Sadot et al. 2005).

7. Bubble competition and merger model predictions

The experimental data were compared to RT bubble competition and merger model predictions. The model describes RT instability growth in the nonlinear regime and was previously described in (Alon et al. 1994; Oron et al. 1998, 2001). The total number N of RT bubbles decreases in time as

$$\frac{\mathrm{d}N}{\mathrm{d}t} = -\sqrt{\frac{g}{\langle\lambda\rangle(t)}}\varpi N(t), \tag{7.1}$$

https://doi.org/10.1017/S0022377814001093 Published online by Cambridge University Press

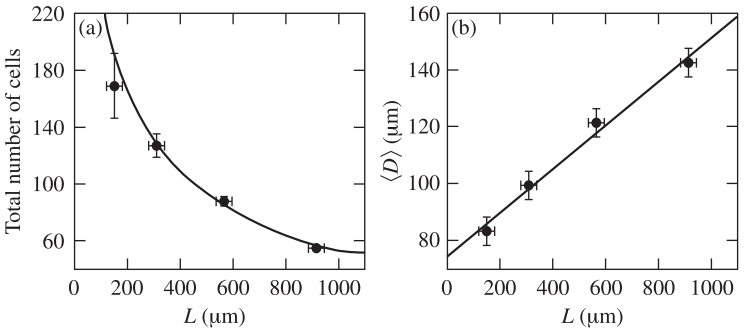


FIGURE 8. (a) Total number of magnetic-field cells and (b) average magnetic-field cell size as a function of the distance traveled by the target. Solid lines are fits to the experimental data based on the predictions from a bubble competition and merger model (Sadot et al. 2005). (Reprinted from Gao et al. (2013) with permission from the American Physical Society. Copyright 2013, APS Publishing LLC.)

where g is the target acceleration, $\langle\lambda\rangle(t)$ is the time-dependent average bubble size, and ϖ is the dimensionless scaled average bubble-merging rate. The average bubble size growth rate is

$$\frac{\mathrm{d}\langle\lambda\rangle}{\mathrm{d}t} = \frac{1}{2}\sqrt{\frac{g}{\langle\lambda\rangle(t)}}\varpi\langle\lambda\rangle(t). \tag{7.2}$$

The solutions to these equations are

$$N(t) = \phi\left(\varpi\sqrt{g}t + 2C\right)^{-4}, \tag{7.3}$$

$$\langle\lambda\rangle(t) = \frac{1}{16}\varpi^2 g t^2 + \frac{1}{4}C\varpi\sqrt{g}t + \frac{1}{4}C^2, \tag{7.4}$$

where $\phi = N_0(2C)^4$, $C = 2\sqrt{\langle\lambda\rangle_0}$, N_0 is the initial number of bubbles, and $\langle\lambda\rangle_0$ is the initial average bubble size. In this model, the nonlinearity produces bubbles and spikes. The modulation evolution is governed by the interaction between neighboring bubbles. In time, bubble competition leads to larger bubbles dominating the system dynamics and the average bubble size shifts to longer wavelengths. As the system develops, the bubble-size distribution evolves self-similarly.

Figure 8 compares the experimental data to the bubble competition and merger model predictions. Figures 8(a) and (b) show the measured total number of magnetic-field cells N_c and the average magnetic-field cell size $\langle D\rangle$ as a function of the distance traveled by the target. The distance traveled by the target is $L = gt^2/2$, where g is the target acceleration, and was measured using side-on proton radiography. This distance determined the amount of RT growth. The experimental data compare well with the scaling $N_c(t) \propto (\varpi_c\sqrt{g}t + 2C)^{-4}$ and $\langle D\rangle \propto \varpi_c^2 g t^2$, where ϖ_c is the scaled magnetic-field cell-merging rate. The self-similarity of the RT growth, where $\langle\lambda\rangle$ grows proportionally to gt^2, is well reproduced in the evolution of the average magnetic-field cell size. The data analysis shows $N_0 = 556 \pm 50$, $\langle D\rangle_0 = 75 \pm 5$ μm, and $\varpi_c = 0.79 \pm 0.06$. This merging rate is in good agreement with the value that was measured in previous nonlinear RT instability studies using similar plastic targets and x-ray radiography (Sadot et al. 2005). In general, the proton radiography data reproduce the bubble competition and merger model predictions, connecting the

https://doi.org/10.1017/S0022377814001093 Published online by Cambridge University Press

spatial distribution and growth of the cellular magnetic-field structures with the RT bubble and spike growth.

8. Summary and conclusions

In summary, experimental results (Gao et al. 2012, 2013) reporting magnetic-field generation during the nonlinear growth of the RT instability in laser-driven foils were reviewed. The MHD evolution of these targets was probed using ultrafast proton radiography, providing detailed maps of the magnetic-field cells that were generated by the ablative nonlinear RT instability. The experiments show, for the first time, self-similar behavior in the growing cellular magnetic-field structures. The data are in good agreement with 2D resistive MHD code calculations and a bubble competition and merger model that predict the time evolution of the number and size of the RT bubbles. Quantitative agreement between the experimental data and the RT model connects the cellular magnetic-field structures with the RT bubble and spike growth. These results are important for understanding the large-scale magnetic-field structures that can be generated in strongly driven flows during hydrodynamic instability growth. At high energy densities, such information is difficult to obtain. These results may be important for understanding the generation of magnetic seed fields in strongly driven plasmas prior to their turbulent amplification, particularly in astrophysical contexts.

Acknowledgments

This material is based upon work supported by the Department of Energy National Nuclear Security Administration under Award Number DE-NA0001944, the University of Rochester, and the New York State Energy Research and Development Authority. The support of DOE does not constitute an endorsement by DOE of the views expressed in this article.

REFERENCES

Alon, U., Hecht, J., Mukamel, D. and Shvarts, D. 1994 Scale invariant mixing rates of hydrodynamically unstable interfaces. *Phys. Rev. Lett.* **72**, 2867–2870.

Atzeni, S. 2004 *The Physics of Inertial Fusion*. Oxford: Clarendon.

Betti, R. and Sanz, J. 2006 Bubble acceleration in the ablative Rayleigh–Taylor instability. *Phys. Rev. Lett.* **97**, 205 002.

Borghesi, M. et al. 2004 Multi-MeV proton source investigations in ultraintense laser-foil interactions. *Phys. Rev. Lett.* **92**, 055 003.

Braginskii, S. I. 1965 *Review of Plasma Physics*. New York: Consultant Bureau.

Clark, E. L. 2001 *PhD thesis,* "Measurements of Energetic Particles from Ultra Intense Laser Plasma Interactions." University of London.

Cowan, T. E. et al. 2004 Ultralow emittance, multi-MeV proton beams from a laser virtual-cathode plasma accelerator. *Phys. Rev. Lett.* **92**, 204 801.

Dimotakis, P. E. 2000 The mixing transition in turbulent flows. *J. Fluid Mech.* **409**, 69–98.

Drake, R. P. 2006 *High-Energy-Density Physics*, Springer/Berlin/Heidelberg.

Evans, R. G. 1986 The influence of self-generated magnetic fields on the Rayleigh–Taylor instability. *Plasma Phys. Control. Fusion* **28**(7), 1021.

Gao, L. 2014 Measurements of magnetohydrodynamic effects in ablatively-driven high energy density systems. *PhD Thesis*, University of Rochester, Rochester NY.

Gao, L. et al. 2013 Observation of self-similarity in the magnetic fields generated by the ablative nonlinear Rayleigh–Taylor instability. *Phys. Rev. Lett.* **110**, 185 003.

Gao, L. et al. 2012 Magnetic field generation by the Rayleigh–Taylor instability in laser-driven planar plastic targets. *Phys. Rev. Lett.* **109**, 115 001.

https://doi.org/10.1017/S0022377814001093 Published online by Cambridge University Press

Haines, M. G. 1986 Magnetic-field generation in laser fusion and hot-electron transport. *Can. J. Phys.* **64**(8), 912–919.

Igumenshchev, I. V., Marshall, F. J., Marozas, J. A., Smalyuk, V. A., Epstein, R., Goncharov, V. N., Collins, T. J. B., Sangster, T. C. and Skupsky, S. 2009 The effects of target mounts in direct-drive implosions on OMEGA. *Phys. Plasmas* **16**(8), 082 701.

Keller, D., Collins, T. J. B., Delettrez, J. A., McKenty, P. W., Radha, P. B., B. Whitney and Moses, G. A. 1999 DRACO – A new multidimensional hydrocode. *Bull. Am. Phys. Soc.* **44**, 37.

Knauer, J. P. et al. 2000 Single-mode, Rayleigh–Taylor growth-rate measurements on the OMEGA Laser System. *Phys. Plasmas* **7**(1), 338–345.

Kugland, N. L., Ryutov, D. D., Plechaty, C., Ross, J. S. and Park, H.-S. 2012 Invited article: Relation between electric and magnetic field structures and their proton-beam images. *Rev. Sci. Instrum.* **83**, 101 301.

Kulsrud, R. M. and Zweibel, E. G. 2008 On the origin of cosmic magnetic fields. *Rep. Prog. Phys.* **71**(4), 046 901.

Lindl, J. 1995 Development of the indirect-drive approach to inertial confinement fusion and the target physics basis for ignition and gain. *Phys. Plasmas* **2**(11), 3933–4024.

Manuel, M. J.-E. et al. 2012 First measurements of Rayleigh-Taylor-induced magnetic fields in laser-produced plasmas. *Phys. Rev. Lett.* **108**, 255 006.

LLE 1987 LLE Quarterly report. *LLE Rev.* **33**, 1–10.

Mima, K., Tajima, T. and Leboeuf, J. N. 1978 Magnetic field generation by the Rayleigh–Taylor instability. *Phys. Rev. Lett.* **41**, 1715–1719.

Nishiguchi, A., Yabe, T. and Haines, M. G. 1985 Nernst effect in laser-produced plasmas. *Phys. Fluids* **28**(12), 3683–3690.

Oron, D., Alon, U. and Shvarts, D. 1998 Scaling laws of the Rayleigh–Taylor ablation front mixing zone evolution in inertial confinement fusion. *Phys. Plasmas* **5**(5), 1467–1476.

Oron, D., Arazi, L., Kartoon, D., Rikanati, A., Alon, U. and Shvarts, D. 2001 Dimensionality dependence of the Rayleigh–Taylor and Richtmyer–Meshkov instability late-time scaling laws. *Phys. Plasmas* **8**(6), 2883–2889.

Orszag, S. A. and Patterson, G. S. 1972 Numerical simulation of three-dimensional homogeneous isotropic turbulence. *Phys. Rev. Lett.* **28**, 76–79.

Rayleigh, L. 1883 Investigation of the character of the equilibrium of an incompressible heavy fluid of variable density. *Proc. Lond. Math. Soc.* **14**, 170.

Remington, B. A. et al. 1997 Supernova hydrodynamics experiments on the Nova laser. *Phys. Plasmas* **4**(5), 1994–2003.

Sadot, O., Smalyuk, V. A., Delettrez, J. A., Meyerhofer, D. D., Sangster, T. C., Betti, R., Goncharov, V. N. and Shvarts, D. 2005 Observation of self-similar behavior of the 3D, nonlinear Rayleigh–Taylor instability. *Phys. Rev. Lett.* **95**, 265 001.

Schneider, M. B., Dimonte, G. and Remington, B. 1998 Large and small scale structure in Rayleigh–Taylor mixing. *Phys. Rev. Lett.* **80**, 3507–3510.

Smalyuk, V. A., Sadot, O., Delettrez, J. A., Meyerhofer, D. D., Regan, S. P. and Sangster, T. C. 2005 Fourier-space nonlinear Rayleigh–Taylor growth measurements of 3D laser-imprinted modulations in planar targets. *Phys. Rev. Lett.* **95**, 215 001.

Srinivasan, B., Dimonte, G. and Tang, X.-Z. 2012 Magnetic field generation in Rayleigh–Taylor unstable inertial confinement fusion plasmas. *Phys. Rev. Lett.* **108**, 165 002.

Taylor, G. 1950 The instability of liquid surfaces when accelerated in a direction perpendicular to their planes. *Proc. R. Soc. A* **201**, 192.

Vincent, L. and Soille, P. 1991 Watersheds in digital spaces: an efficient algorithm based on immersion simulations. *IEEE Trans. Pattern Anal. Mach. Intell.* **13**, 583.

Waxer, L. J. et al. 2005 High-energy petawatt capability for the Omega Laser. *Opt. Photon. News* **16**(7), 30–36.

Wilks, S. C. et al. 2001 Energetic proton generation in ultra-intense laser-solid interactions. *Phys. Plasmas* **8**(2), 542–549.

Willingale, L. et al. 2009 Characterization of high-intensity laser propagation in the relativistic transparent regime through measurements of energetic proton beams. *Phys. Rev. Lett.* **102**, 125 002.

Zylstra, A. B. et al. 2012 Using high-intensity laser-generated energetic protons to radiograph directly driven implosions. *Rev. Sci. Instrum.* **83**(1), 013 511.

https://doi.org/10.1017/S0022377814001093 Published online by Cambridge University Press

Culham Prize Winner 2006



Dr. Philip Nilson studies high energy density physics at the University of Rochester's Laboratory for Laser Energetics (LLE). He graduated with a 1st class honours degree in physics (MPhys) from the University of Warwick and earned his PhD in physics from Imperial College, London. Philip was awarded the Culham PhD Thesis Prize in 2006 for measurements of the dynamics of laser and soft x-ray heated targets by XUV and optical probing. In 2006, Philip joined the University of Rochester's Fusion Science Center for Extreme States of Matter as a postdoctoral researcher studying intense radiation-matter interactions. Philip became a member of the Experimental Physics Division at LLE in 2008. Since 2008, Philip's research has focused on the study of intense-energy coupling and ultrafast energy transport in plasmas, shock-wave propagation, and hydrodynamic instability growth. In addition to these research activities, Philip is a graduate student advisor for doctoral candidates in the Physics and Mechanical Engineering Departments at the University of Rochester.

https://doi.org/10.1017/S0022377814001093 Published online by Cambridge University Press